Direct Syngas-To-Ethanol Conversion over Lithium-Promoted Rh/MgO Catalysts

Ait El Fakir, Abdellah; Du, Pengfei; Wan, Li; Pan, Hong Li; Zhao, Shirun; Dostagir, Nazmul Hasan M.D.; Pidko, Evgeny A.; Shimizu, Ken Ichi; Toyao, Takashi; More Authors

DOI
10.1021/acscatal.4c05085

Publication date
2025

Document Version
Final published version

Published in
ACS Catalysis

ACS Catalysis

pubs.acs.org/acscatalysis Research Article

Direct Syngas-To-Ethanol Conversion over Lithium-Promoted Rh/MgO Catalysts

Abdellah Ait El Fakir,[‖] Pengfei Du,[‖] Li Wan, HongLi Pan, Shirun Zhao, Nazmul Hasan M.D. Dostagir, Akihiko Anzai, Shinya Mine, Evgeny A. Pidko, Ken-ichi Shimizu,* and Takashi Toyao*

Cite This: *ACS Catal.* 2025, 15, 2033−2044 Read Online

ACCESS | Metrics & More | Article Recommendations | Supporting Information

ABSTRACT: Significant efforts have been dedicated to the direct syngas conversion into ethanol, however, achieving a high ethanol yield remains a formidable task. In this study, we present the direct syngas-to-ethanol conversion over Li-promoted RhO_x/MgO catalyst (RhO_x/Li_2O/MgO). The ethanol space-time yield (EtOH STY) and selectivity reached 12.2 mmol g_{cat}^{-1} h^{-1} and 20%, respectively, at a 35% CO conversion over the RhO_x/Li_2O/MgO catalyst. The RhO_x/Li_2O/MgO catalyst demonstrated superior performance in terms of both ethanol selectivity and STY compared to Rh/Li_2O catalysts on other support materials and Rh/MgO catalysts promoted with other alkali metals. In situ/operando spectroscopic techniques, combined with other characterisations and theoretical calculations, have elucidated the interactions between Li_2O and Rh on the MgO surface. These interactions promote the formation of new active sites and weaken CO adsorption on the Rh surface, thereby enhancing ethanol production. This work provides a promising strategy for improving ethanol yield in syngas conversion processes.

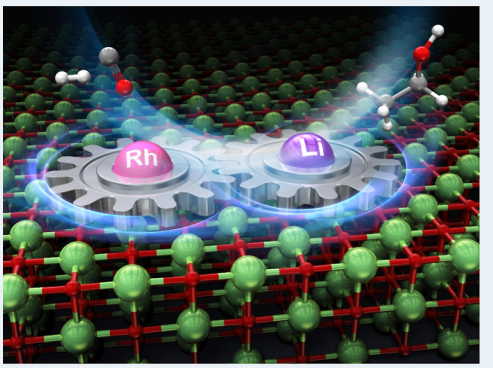

KEYWORDS: *syngas conversion, Rh-based catalysts, ethanol synthesis, Li promotion, support effect*

1. INTRODUCTION

The ever-increasing demand for crude oil has caused a notable reduction in oil reserves worldwide. Recently, to reduce the dependency on oil, considerable attention has been directed toward the efficient use of shale gas, coal, natural gas, and biomass. Syngas (CO + H_2), produced from various sources including natural gas, carbon dioxide, coal, biomass, and carbon-rich waste materials, is a viable precursor for high-value products.[1−9] Consequently, the direct higher oxygenates (C_{2+} oxy) synthesis from syngas has a significant impact on converting biomass, methane, organic waste, and coal into high-value chemicals and clean liquid transportation fuels.[10−12] Supported catalysts play an important role in this field, particularly in higher alcohol (HA) synthesis.[13−21] The pronounced interaction between nanomaterials and support materials has been extensively investigated to elucidate the structure−activity relationship in oxide-supported metal catalysts.[5,6,19,22−24] Notably, noble metals exhibit a remarkable synergy with metal oxide supports, modulating CO and H_2 adsorption and activation at elevated reaction temperatures. The supported Rh catalysts exhibit notable activity and selectivity for ethanol production than alternative syngas conversion catalysts.[25−35]

The choice of catalyst support and the introduction of various promoters to Rh catalysts are critically important for achieving high ethanol and hydrocarbon (HC) yields. Among the various promoter elements explored, alkali metals were found to be effective in improving both the CO conversion and the ethanol formation over Rh catalysts.[25−27] Alkali metals stabilize partially oxidized Rh clusters and modulate the dispersion and electronic structure of Rh nanoparticles, thereby serving as structural and electronic promoters to fine-tune the catalytic activity.[36,37] Alkali metals can prevent the hydrogenation of CH_x* and alkylation reactions, thereby reducing CH_3OH and CH_4 formation, and increasing the formation of C_{2+} oxygenates.[38,39] The ability of Rh catalysts to catalyze CO dissociation, CO insertion, and hydrogenation is influenced by both the addition of the alkali promoter and the choice of support material.[40] The variation in the support materials indicates that the products selectivities in CO hydrogenation can be significantly altered,[22,40] with surface hydroxyl groups also playing a crucial role in the C_{2+} oxygenates synthesis on Rh-based catalysts.[41,42] Many studies focusing on SiO_2 and TiO_2 supports have concluded that their high surface area, pronounced porosity, and stability collectively contribute to enhanced selectivity toward C_{2+} oxygenates.[35,43−45] Additionally, γ-Al_2O_3 has been recognized

Received: August 23, 2024
Revised: January 1, 2025
Accepted: January 9, 2025

https://doi.org/10.1021/acscatal.4c05085
ACS Catal. 2025, 15, 2033−2044

as an effective support for transition metal catalysts for both CO and CO_2 hydrogenation to C_{2+} oxygenates, due to its high specific surface area and porosity, which promote optimal dispersion of metal particles.[24,46] Furthermore, supports such as ZrO_2[47,48] and CeO_2[49] have been reported for their catalytic properties in similar applications.

This study focused on using MgO as an unconventional support for Rh nanoparticles in the hydrogenation of CO to EtOH. We demonstrate that the introduction of the Li promoter has an impact on the surface structure and enhances the activity and ethanol production over MgO-supported Rh catalysts. Through comparative analyses with established catalysts, this study aims to explain the mechanistic disparities underlying the superior performance of the $Rh/Li_2O/MgO$ catalysts. Notably, $Rh/LiO_x/MgO$ catalysts exhibit an ethanol space-time yield (EtOH STY) of 12.2 mmol g_{cat}^{-1} h^{-1}. The comprehensive experimental investigations, including in situ/operando spectroscopic techniques complemented by density functional theory (DFT) calculations, provided insights into the active sites and reaction mechanisms of the Rh/LiOx/MgO catalyst.

2. MATERIALS AND METHODS

2.1. Catalysts Preparation. MgO was supplied by Ube Materials Industries, Ltd. TiO_2 (P25) was obtained from Evonik (Denmark). SiO_2 was purchased from Fuji Silysia Chemical Company Ltd. γ-Al_2O_3 (Puralox) was obtained from Sasol. Rh and Li were introduced through a sequential impregnation method. An aqueous solution (30 mL) of $LiNO_3$ (Wako Pure Chemical Industries, >99.5%) and 0.97 g of support were introduced to a 100 mL glass vessel. The slurry was stirred and dried at 50 °C. After drying overnight at 90 °C, the samples were calcined for 3 h at 500 °C to obtain alkali metal/support (Li_2O/MgO, Li_2O/TiO_2, Li_2O/Al_2O_3, Li_2O/SiO_2). A 0.98 g sample of Li_2O/support and 0.4 mL of an aqueous $Rh(NO_3)_3$ solution (50 g/L, Furuya Metal Co., Ltd.) were combined in a 100 mL glass vessel containing 30 mL of deionized water. The mixture was stirred, then evaporated to dryness at 50 °C. After evaporation, the sample was further dried at 110 °C for 12 h to obtain the supported Rh/Li catalysts, labeled as $Rh_2O_3/Li_2O/MgO$, $Rh_2O_3/Li_2O/TiO_2$, $Rh_2O_3/Li_2O/Al_2O_3$, $Rh_2O_3/Li_2O/SiO_2$, respectively. The catalyst was synthesized using the impregnation method at a calcination temperature of 500 °C. Therefore, the introduced Li and Rh species would be supported as introduced. The Rh loading in our catalysts is 2 wt %, while the loading of Li and other alkali metals is 3 wt %.

2.2. Catalysts Characterization. The structural characterization was carried out for both reduced and spent catalysts. For the reduced catalyst, characterization was conducted after 30 min of H_2 pretreatment, while for the spent catalyst, characterization was carried out after a standard reaction time of 24 h, which included 12 h of aging at 360 °C and 12 h of reaction testing with a temperature range of 240 to 360 °C.

X-ray diffraction (XRD) analysis was measured on a Rigaku Miniflex diffractometer from 20 to 70° (scan speed of 5°/min) with Cu Kα monochromatic radiation (λ = 0.154 nm). High-angle annular dark-field scanning transmission electron microscopy (HAADF-STEM) coupled with energy-dispersive X-ray spectroscopy (EDX) were measured using a FEI Titan G2 microscope.

Rhodium K-edge X-ray absorption spectroscopy (XAS) experiments were conducted via transmission mode at the BL01B1 beamline of SPring-8 housed within the Japan Synchrotron Radiation Research Institute (JASRI) under Proposal no. 2023B2096/2023A1931. The experiments were conducted using a Si(311) double-crystal monochromator. In addition, the reference compound spectra were recorded under ambient conditions at room temperature. The acquired XAS results were analyzed with Athena and Artemis software, version 0.9.26, both integrated within the Demeter package.[50]

For Rh K-edge in situ X-ray absorption near-edge structure (XANES) investigations, the prepared catalyst pellet (7 mm diameter) was placed in a cell fitted with Kapton film windows and a microgas chromatograph (GC) was equipped at the outlet for exhaust gas analysis. The transmission mode was used to conduct these measurements. The Rh foil spectra were collected simultaneously for energy calibration. In a typical experiment, initial X-ray absorption fine structure (XAFS) scans were performed using the catalyst at room temperature under He flow. Following H_2 reduction (100 mL/min) at 360 °C for 30 min, XANES results were acquired. And then, the gas feed was then transitioned to He (300 mL/min), CO (100 mL/min), and CO (33.3 mL/min) + H_2 (66.7 mL/min), in succession, while maintaining a temperature of 360 °C.

Operando diffuse reflectance infrared Fourier transform (DRIFT) spectra were obtained using a JASCO FT/IR-4600 instrument, which was equipped with a mercury cadmium telluride (MCT) detector. Spectra were collected at a resolution of 8 cm^{-1} under 5 bar pressure and 320 °C. Each spectrum was corrected by subtracting a reference spectrum recorded under He flow at the measurement temperature. Methanol and ethanol analyses were performed using a high-sampling-rate TCD GC (490 Micro GC; Agilent Technologies Inc.) installed at the reaction cell outlet.

Temperature-programmed reduction with H_2 (H_2-TPR) was conducted using a BELCAT II instrument equipped with a TCD. About 100 mg of the catalyst was placed in a quartz tube and purged with Ar at 200 °C for 2 h to eliminate physically adsorbed surface carbonates and water. After cooling the sample to 50 °C, it was gradually heated to 800 °C under a flow of 10 vol % H_2 balanced with Ar.

H_2 chemisorption was measured using a BELCAT II instrument with a TCD to determine the number of exposed Rh surface atoms. 0.1 g portion of the catalyst samples was initially reduced first at 360 °C under the hydrogen for 30 min, then evacuated at 400 °C for an additional 30 min. The sample was then cooled under vacuum to 40 °C and further cooled to −60 °C before recording the H_2 adsorption isotherm. The metal dispersion and turnover frequency (TOF) were calculated assuming H/Rh_s = 1.[37]

The CO_2 temperature-programmed desorption (CO_2-TPD) reaction was conducted using a BELCAT II instrument connected to a TCD to evaluate the basicity of the prepared catalysts. For this test, a 100 mg catalyst powder was reduced at 360 °C under H_2 flow. The catalyst was preheated to 400 °C for 10 min prior to testing to eliminate any potential impurities. The sample was then cooled to 40 °C and subjected to a 30 mL/min CO_2 flow for 30 min to fully saturate the surface. Following this, a 30 mL/min He flow was applied for 30 min to remove any physically adsorbed CO_2. After these pretreatments, the catalyst was heated at a temperature rate of 10 °C/min from 50 to 700 °C to collect CO_2 desorption data.

The Fourier-transform infrared spectroscopy (FTIR) spectra of adsorbed CO were recorded in transmission mode using a

https://doi.org/10.1021/acscatal.4c05085
ACS Catal. 2025, 15, 2033−2044

JASCO FTIR-4600 equipped with an MCT detector. A 70 mg portion of the catalyst was formed into a pellet and placed into a quartz cell with CaF_2 windows, surrounded by a Dewar vessel. After purging with He for several minutes, the feed gas was changed to H_2 (20 mL/min) for reduction at 360 °C for 30 min. Following this, the gas flow was changed back to He, and the catalyst was cooled to −20 °C using a liquid nitrogen and ethanol mixture. After recording the background spectrum, the catalysts were exposed to a 10% CO/He (15 mL/min) at 1 bar, followed by He (50 mL/min) to purge CO in the gas phase, which was physisorbed onto the catalyst.

2.3. Catalytic Reactions. Syngas conversion experiments were carried out in a fixed-bed reactor maintained at a pressure of 3 MPa. A gas mixture of H_2/CO/Ar with a ratio of 66.1/33.1/0.8 was introduced into the reactor, using Ar as an internal standard. Initially, 70 mg of the catalyst was placed in a fixed-bed reactor with an inner diameter of 1/4 in. The catalyst was subjected to pretreatment at ambient pressure with a 99% H_2/Ar flow at a rate of 15 mL/min, maintaining a temperature of 360 °C for 30 min. Following pretreatment, a gas mixture of H_2/CO/Ar (66.1/33.1/0.8) with a total flow rate of 30 mL/min was introduced into the catalyst bed at a pressure of 30 bar to attain a space velocity (SV) of 25,700 mL g^{-1} h^{-1}. An aging treatment was applied for 12 h at 360 °C under reaction conditions as an accelerated aging test before recording the catalytic reaction results (Figure S1). Product analysis was performed using an online gas chromatograph (Shimadzu GC-2014) equipped with thermal conductivity (TCD) and flame ionization (FID) detectors, within a reaction temperature range of 240−360 °C.

The CO conversion (X_{CO})

$$X_{CO} = \frac{n_{CO}^{in} - n_{CO}^{out}}{n_{CO}^{in}} \times 100\%$$

Selectivity (S_i) for each product

$$S_i = \frac{c_i \times n_i}{\sum (c_i \times n_i)} \times 100\%$$

C_i represents the molar fraction of product i (CO_2, HC, or oxygenates), and n_i represents the carbon number of products i.

2.4. DFT Calculations. Vienna Ab Initio Simulation Package (VASP, version 5.4.4) was used for the periodic DFT calculations.[51,52] The Perdew−Burke−Ernzerh of functional revised for solids (PBEsol) was utilized along with the projector-augmented wave method.[53,54] A plane-wave basis set with a cutoff energy of 400 eV was applied, and a Gaussian smearing of 0.2 eV was used to distribute the electronic states. Only the gamma point (1 × 1 × 1) was considered in the k-point grid. van der Waals interactions were described using a dispersion-corrected DFT-D3 (BJ) function.[55] The force convergence criterion for each atom was set to 0.03 eV $Å^{-1}$.

Supercell slab models were used to simulate the MgO (100) surface (Figure S2a).[56] where the slabs were repeated along the surface-normal direction and separated by a vacuum region of at least 15° (lattice parameters for the surface: a = 16.78 Å, b = 16.78 Å). The two bottom layers were fixed at their original bulk positions. One layer of $Li_2O(111)$ was attached to the MgO(100) surface to model the $Li_2O(111)$/MgO(100) surface (Figure S2b). Given that the Brunauer−Emmett−Teller (BET) specific surface area of the MgO support used in this study was 50 m^2/g and the Li loading was 3 wt %, if Li_2O uniformly covered the surface of the MgO support, it formed a monolayer. Based on this, we modeled the $Li_2O(111)$/MgO(100) surface. To simulate Rh nanoparticles on the supports, a Rh_{13} cluster was employed. This Rh_{13} cluster was placed on a pristine MgO(100) surface (Rh_{13}/MgO(100)) as well as on $Li_2O(111)$/MgO(100) (Rh_{13}/$Li_2O(111)$/MgO-(100)), as shown in Figure 1.

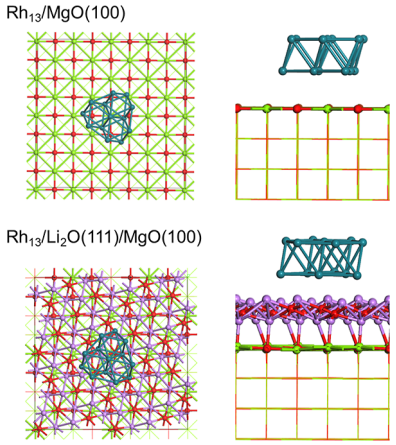

Figure 1. Slab models are used for DFT calculations of the Rh_{13}/MgO(100) and Rh_{13}/$Li_2O(111)$/MgO(100) surfaces. Rh, Li, Mg, and O atoms are presented as dark green, purple, light green, and red.

The adsorption energy (E_{ads}) of a CO molecule on a surface is defined as

$$E_{ads} = E_{A/S} - E_A - E_S$$

where $E_{A/S}$, E_A, and E_S represent the electronic energies of the adsorption complex, free-state adsorbate, and the bare metal oxide surface, respectively.

3. RESULTS AND DISCUSSION

3.1. Catalytic CO Hydrogenation to EtOH. The catalytic performance of various Rh-based catalysts was evaluated in a fixed-bed reactor under conditions of 320 °C, a weight hourly space velocity of 25,700 mL g^{-1} h^{-1} and 3 MPa. As evident from the accompanying Figure 2a and Table S1, the unpromoted RhO_x/MgO showed methanol selectivity of 17.7% at 320 °C, whereas selectivities for other products such as methane, ethanol, and higher alcohols were 28.9%, 5.3%, and 8.2%, respectively. Methanol formation involves a nondissociative mechanism at sites capable of hydrogenating the adsorbed CO.[40,57] Therefore, the increased total selectivity of the C1 species (methanol) for RhO_x/MgO suggests both a low CO insertion activity and adequate hydrogenation activity for conversion into C1 products. The addition of alkali metals (K, Li, Cs, and Na) increased the ethanol selectivity (Figure 2a) from 5.3% for RhO_x/MgO to 9.2%, 10.4%, 10.9%, and 20% for RhO_x/Na_2O/MgO, RhO_x/K_2O/MgO, RhO_x/Cs_2O/MgO, and RhO_x/Li_2O/MgO, respectively. For RhO_x/Na_2O/MgO catalyst, we observe that CO_2 selectivity is higher than that in the other catalysts. This can be due to increased CO_2 production through enhanced WGS reaction facilitated by Na addition as reported.[39] Notably, the catalyst promoted by Li exhibited the highest ethanol yield, increasing from 4.8 mmol g_{cat}^{-1} h^{-1} for RhO_x/MgO to 12.2 mmol g_{cat}^{-1} h^{-1} for RhO_x/Li_2O/MgO, with a corresponding increase in CO conversion from 20.5% to 36.4%. The production of $C_{2+}OH$

https://doi.org/10.1021/acscatal.4c05085
ACS Catal. 2025, 15, 2033−2044

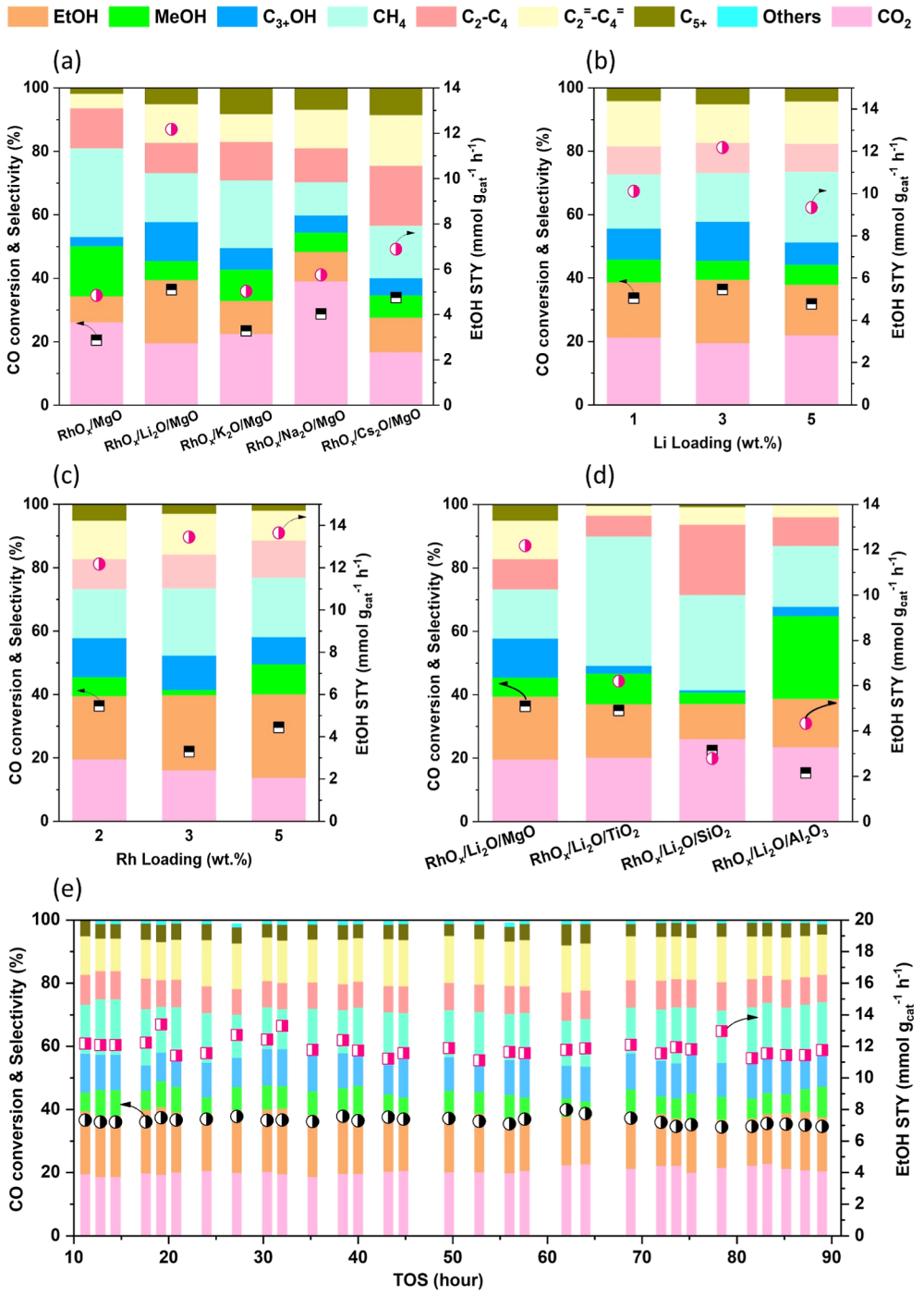

Figure 2. Catalytic performance. (a) Product selectivity and EtOH STY on different alkali metals-RhO_x/MgO; product selectivity and EtOH STY on different (b) Li loading (c) and Rh loading. (d) Product selectivity and EtOH STY on RhO_x/Li_2O/supports (Others, including formate and acetaldehyde). (e) Stability of RhO_x/Li_2O/MgO at 320 °C, 25,700 mL g_{cat}^{-1} h^{-1}, 3.0 MPa, conditions: 70 mg catalyst, H_2/CO as 2 by volume, and Ar as internal standard (0.8 vol %).

products was observed at the expense of the C_1 products (CO_2, methane, and methanol), which was attributed to the influence of Li on the CO dissociation ability of RhO_x/MgO.[37] Analysis of the effect of the Li loading on the performance, as shown in Figure 2b, revealed that 3 wt % Li yielded optimal rates and selectivity, reaching 12.2 mmol g_{cat}^{-1} h^{-1} and 20%, respectively. Figure 2c shows the effect of Rh loading on the performance. An increase in the Rh loading from 2 wt % to 5 wt % increases the formation rate and selectivity to 13.8 mmol g_{cat}^{-1} h^{-1} and 25%, respectively. However, we chose to use 2 wt % due to the high cost of Rh. We further examined the reaction conditions influences, containing temperature, pressure, and WHSV, on the EtOH synthesis (Figure S3a,b). Varying the reaction temperature from 240 to 360 °C revealed that both the EtOH STY and C_{2+} alcohol distribution followed a typical volcano-shaped curve with a maximum at approximately 320 °C. The reaction pressure was varied between 3 and 5 MPa, with the highest EtOH STY (12.2 mmol g_{cat}^{-1} h^{-1}) achieved at 3 MPa. Additionally, we investigated the influence of WHSV by varying it between

https://doi.org/10.1021/acscatal.4c05085
ACS Catal. 2025, 15, 2033−2044

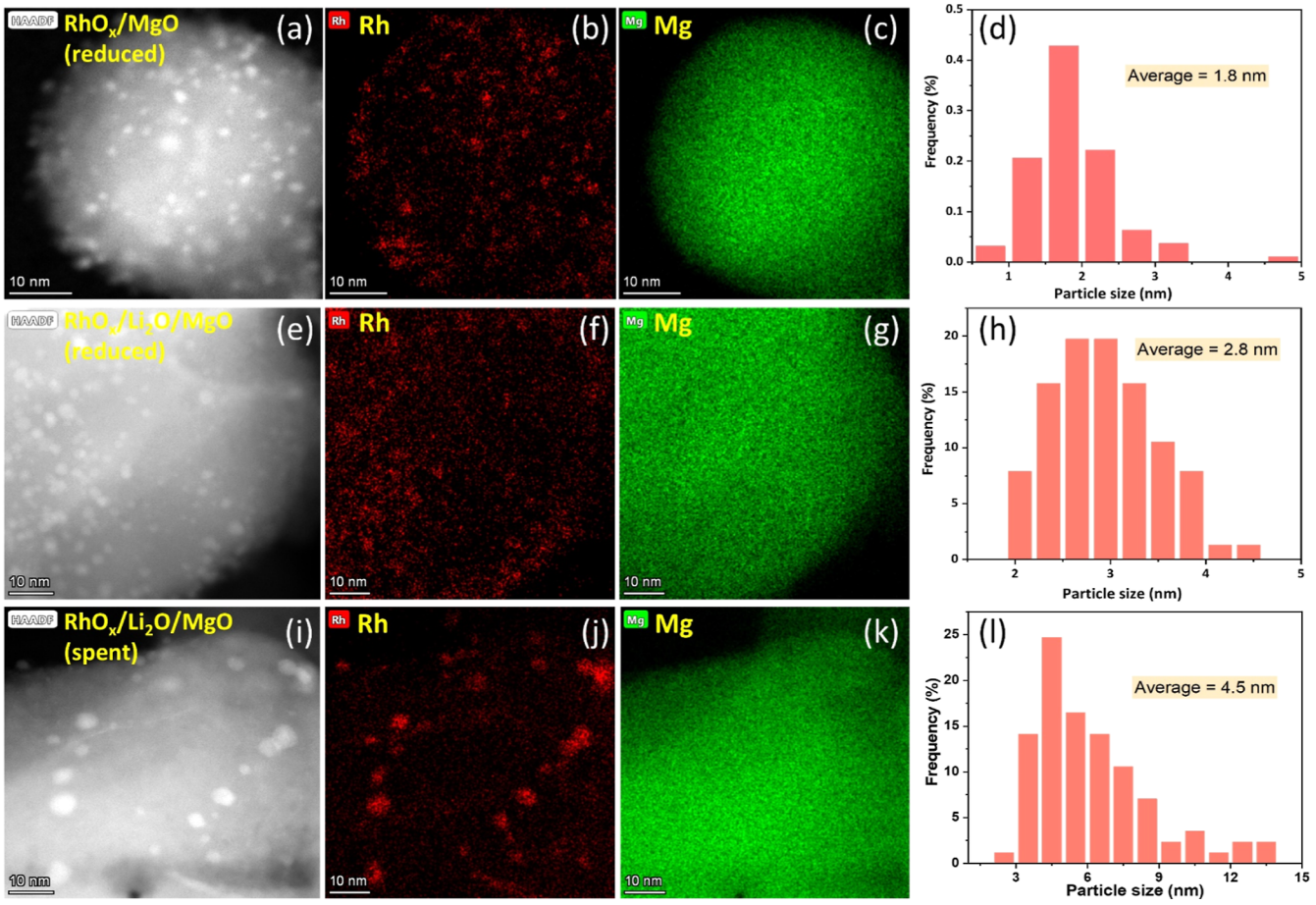

Figure 3. HAADF-STEM images (a,e,i), corresponding EDX mapping images (b,c,f,g,j,k), and particle size distribution (d,h,l) of the RhO_x/MgO, $RhO_x/Li_2O/MgO$ (reduced samples) and $RhO_x/Li_2O/MgO$ (spent sample).

25,700 and 51,000 mL g_{cat}^{-1} h^{-1}, finding that the higher WHSV led to a higher ethanol yield.

The catalytic activity of the Rh catalysts for CO dissociation, insertion, and hydrogenation was influenced by the presence of alkali promoter and support material.[58,59] MgO is a promising electronic or structural promoter for facilitating the high-yield synthesis of methanol via direct CO hydrogenation, achieved through combined reverse water−gas shift (RWGS) and Fischer−Tropsch synthesis (FTS) processes.[60−63] Despite this potential, investigations on MgO-promoted Rh catalysts remain limited. In addition, comprehensive studies exploring the relationship between the distinct catalyst support structures and their activities are lacking. Figure 2d shows the effect of support, such as MgO, TiO_2, Al_2O_3, and SiO_2 on syngas to ethanol conversion. The $RhOx/Li_2O/MgO$ catalyst exhibited the best performance, highlighting the effectiveness of MgO in ethanol production. The catalytic stability of $RhO_x/Li_2O/MgO$ was evaluated over a 90 h reaction period under the optimized conditions (Figure 2e), revealing no significant changes in CO conversion, product selectivity, and EtOH STY, suggesting that the $RhO_x/Li_2O/MgO$ catalyst maintains stable performance. For comparison, we also summarized the literature data on syngas conversion to ethanol over various catalysts in Table S2. Notably, the selectivity and formation rate of $C_{2+}OH$ and EtOH achieved in this study rank among the highest compared to those of representative catalysts reported in the existing literature.

3.2. Structural Characterization. HAADF-STEM was used to characterize the supported Rh nanoparticles. Figure 3 displays the HAADF-STEM images of RhO_x/MgO and $RhO_x/Li_2O/MgO$ (reduced samples) coupled with X-ray EDS for elemental analysis. The Rh species exhibited a uniform distribution on both catalysts (Figures 3a,e and S4 and S5), with the introduction of a promoter resulting in a subtle increment in particle size with an average of 1.8 to 2.8 nm. Elemental mapping demonstrated the homogeneous distribution of Rh across the catalyst surface, confirming the colocalization of Rh and Mg (Figure 3b−d,f−h). We also characterized the spent $RhO_x/Li_2O/MgO$, and the results are presented in Figures 3i and S6. HAADF-STEM resolved larger particles ranging from 2.8 to 13 nm with an average of 4.5 nm and were discernible in the spent catalyst, which was absent in the reduced catalyst (before the reaction), suggesting their formation through sintering during the catalytic reaction. The STEM-EDS elemental mappings (Figure 3j−l) reveal a consistent distribution of Rh throughout the MgO support. Table S3 summarizes the results from H_2 chemisorption. Although agglomeration of Rh nanoparticles was observed before and after the reaction, H_2 chemisorption data showed that the number of active sites determined based on the H_2 chemisorption experiment remained almost unchanged, resulting in almost the same TOF values (0.015 s^{-1} for the fresh catalyst and 0.016 s^{-1} for the spent catalyst).

The HAADF-STEM characterization was performed on $RhO_x/Li_2O/SiO_2$, $RhO_x/Li_2O/TiO_2$ and $RhO_x/Li_2O/Al_2O_3$

https://doi.org/10.1021/acscatal.4c05085
ACS Catal. 2025, 15, 2033−2044

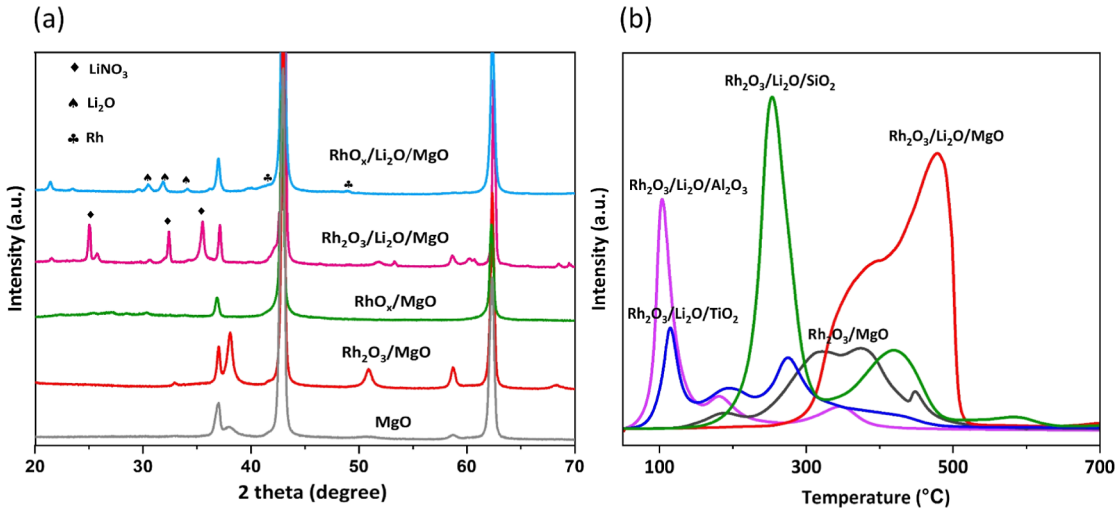

Figure 4. (a) XRD patterns of various MgO based catalysts; (b) H_2-TPR results over different control catalysts. Condition: Ar pretreatment at 200 °C for 1 h, heating in 10% H_2/Ar from 50 to 700 °C.

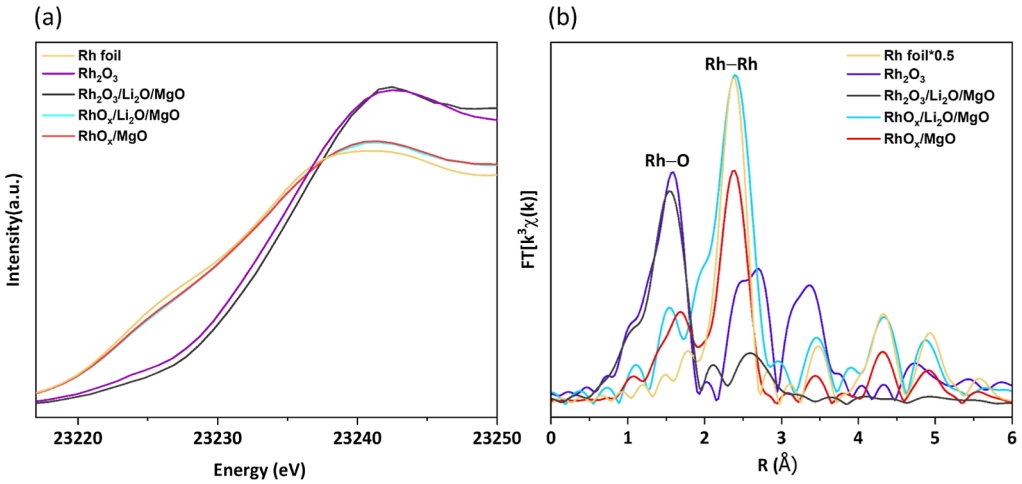

Figure 5. XAS results. (a) Rh K-edge XANES measurements; (b) comparison of the Fourier transform (FT) of Rh K-edge k_3-weighted EXAFS oscillations for the $Rh_2O_3/Li_2O/MgO$ (unreduced sample), $RhO_x/Li_2O/MgO$ and RhO_x/MgO (reduced samples).

after H_2 reduction. As shown in Figure S7, the particle sizes of all supported Rh catalysts exhibit slight differences, with average sizes of 1.85, 1.99, and 1.57 nm for $RhO_x/Li_2O/SiO_2$, $RhO_x/Li_2O/TiO_2$, and $RhO_x/Li_2O/Al_2O_3$ catalysts, respectively. STEM-EDS elemental mapping indicated that the Rh atoms were homogeneously distributed across the catalyst surfaces.

The presence of crystalline phases within the catalyst was examined after calcination, H_2 reduction, and the reaction using XRD, as shown in Figure 4a. The XRD pattern contains peaks associated with MgO.[64] Analysis of the peaks formed after Li loading showed that the Li species in the catalyst existed as Li_2O. In addition, The Rh_2O_3/MgO and $Rh_2O_3/Li_2O/MgO$ (unreduced sample) catalysts are indicative of the absence of crystalline structures corresponding to Rh_2O_3 or metallic Rh. This is due to the high dispersion of Rh, rendering the crystalline domains below the detection limit of the instrument. After H_2 reduction, changes in the crystal structure were observed, with patterns indicating the presence of the Rh crystal phase but not oxidized Rh_2O_3 as shown in the XAS analysis (this will be discussed in a later section). Similar observations were made for the spent catalyst, where Rh metal diffraction peaks were present, albeit larger particles were observed in the STEM analysis. The XRD pattern of the alternative support exhibits similar results, indicating the absence of crystalline structures corresponding to Rh (Figure S8). This is attributed to the high dispersion of the Rh species within the material.

The CO_2 TPD experiments were employed to study the basicity of the catalysts, and the results are given in Figure S9. The addition of Li to the MgO support enhanced its basicity, as indicated by an increased intensity of the CO_2 desorption peak and the appearance of a new peak at higher temperature that indicates the formation of the strong basic sites.

H_2-TPR was employed to study the reducibility of the catalysts, and the results are summarized in Figure 4b. The MgO support plays a critical role in influencing the reduction behavior of Rh-based catalysts.[65−67] It is known that supported metals become more difficult to reduce on basic supports such as MgO.[67,68] When Li is introduced into the MgO support, as in the $Rh_2O_3/Li_2O/MgO$ catalyst, the reducibility of Rh is further hindered, with the reduction temperature shifting to an even higher value (370 °C). This indicates that Li introduction enhances the basicity of the MgO support (figure S9). In

https://doi.org/10.1021/acscatal.4c05085
ACS Catal. 2025, 15, 2033−2044

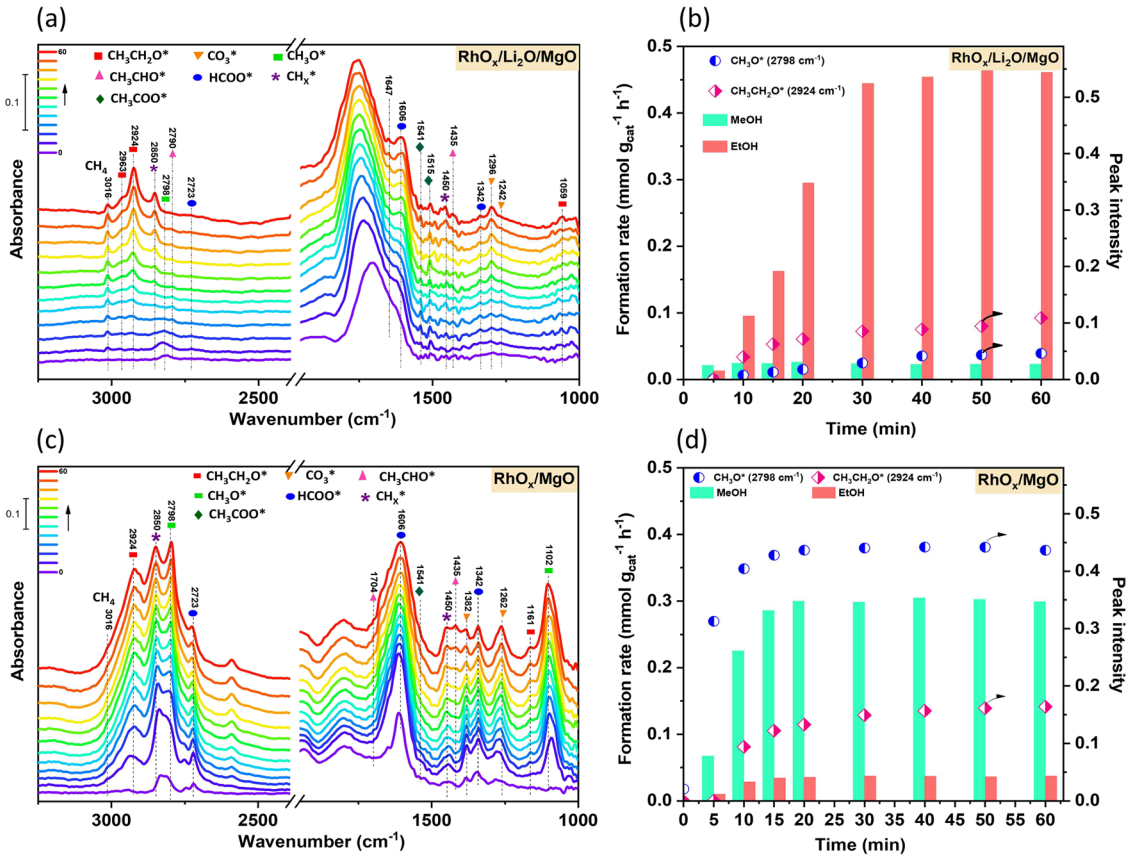

Figure 6. Operando DRIFT spectra of CO hydrogenation over the $RhO_x/Li_2O/MgO$ (a) and RhO_x/MgO (c) catalysts. Dynamic IR peak intensities of $CH_3CH_2O^*$ and CH_3O^* and formation rate resulted from Micro GC over the $RhO_x/Li_2O/MgO$ (b) and RhO_x/MgO (d) catalysts. Reaction conditions: 0.5 MPa, CO/H_2 = 1/2, 30 mL min^{-1}, and 320 °C.

contrast, supports with lower basicity, such as SiO_2, TiO_2, and Al_2O_3, allow for easier reduction, as evidenced by the lower reduction temperatures (270 °C for $Rh_2O_3/Li_2O/SiO_2$ and around 100 °C for $Rh_2O_3/Li_2O/TiO_2$ and $Rh_2O_3/Li_2O/Al_2O_3$). Therefore, the reduction capability follows the order: $Rh_2O_3/Li_2O/MgO < Rh_2O_3/Li_2O/SiO_2 < Rh_2O_3/Li_2O/TiO_2 \approx Rh_2O_3/Li_2O/Al_2O_3$.

XAS was further employed to indicate the role of the Li promoter on the reducibility, environment, and oxidation state of Rh. Ex situ XANES spectra of the Rh K-edge of the Rh catalysts are shown in Figure 5a. $Rh_2O_3/LiO_2/MgO$ (unreduced sample) clearly indicated the presence of cationic Rh (Rh_2O_3). EXAFS spectra revealed Rh−O scattering paths, with Rh−O contributions at 2.05 Å (Table S4).[46−48] The formation of metallic Rh is observed after the treatment with H_2 at 360 °C for 30 min as evidenced by the shift of the absorption edge to lower energies for both $RhO_x/Li_2O/MgO$ and RhO_x/MgO catalysts (reduced samples). The XANES and EXAFS spectra of these materials are different from those of the Rh foil, which we attribute to the presence of some remaining unreduced cationic Rh or to charge transfer between the metal and the support.[25,37,46] Figure 5b and Table S4 summarize the curve-fitting results for the EXAFS data for all the measured catalysts. The coordination number (CN) values obtained for the Rh−Rh shells of both the unpromoted and promoted Li-promoted RhO_x/MgO catalysts after H_2 reduction were lower than the bulk value, suggesting the formation of small Rh particles. The high dispersion of Rh is also in line with the observed decrease in the coordination distance relative to the bulk value (R = 2.69 Å). The presence of the promoter resulted in a slight increase in the particle size, as evidenced by the larger CN values in the EXAFS fits and STEM results. The Rh particle size can be estimated using Rh cluster models with different numbers of atoms to calculate the average CN.[69,70] The estimated Rh particle size is approximately 0.9 nm (CN: 5.3) for RhO_x/MgO and around 1.3 nm (CN: 6.5) for $RhO_x/Li_2O/MgO$. However, it is important to note that the presence of minor Rh^+ species and the geometric shape of the particles influence the particle size calculation, potentially accounting for the discrepancy with the STEM particle size distribution. Nevertheless, both characterization methods indicate the same trend: Rh particle size increased after Li loading.

3.3. Mechanistic Studies. The operando DRIFTS connected with mass spectrometry outlet was used to investigate the mechanism governing the CO hydrogenation to EtOH under working conditions at 320 °C, 0.5 MPa, and a H_2/CO ratio of 2 on $RhO_x/Li_2O/MgO$ and RhO_x/MgO catalysts and other reference catalysts. The results (Figure 6a) for the Li promoted catalyst ($RhO_x/Li_2O/MgO$) reveals the band at 3016 cm^{-1} corresponding to the C−H stretching vibration in CH_4,[39,71] and the gradual buildup of the bands due to C−H bond asymmetric stretching (ν_{as} C−H) and asymmetric bending (δ_{as} C−H) vibration in CH_x* at approximately 2850 and 1450 cm^{-1}. The band ν(C═O), corresponding to the vibrations of carbonyl groups in aldehydes, was observed at 1704 cm^{-1}, along with the bands at 2790 and 1435 cm^{-1} were recorded, which are consensually

https://doi.org/10.1021/acscatal.4c05085
ACS Catal. 2025, 15, 2033−2044

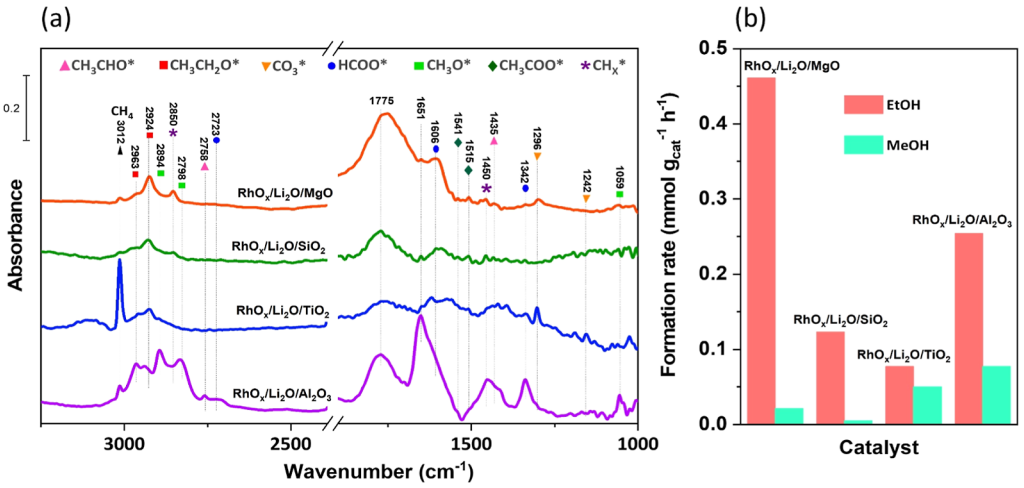

Figure 7. (a) Operando DRIFT spectra of CO hydrogenation over the $RhO_x/Li_2O/MgO$, $RhO_x/Li_2O/TiO_2$, $RhO_x/Li_2O/SiO_2$ and $RhO_x/Li_2O/Al_2O_3$ catalysts. Reaction conditions: 0.5 MPa, CO/H_2 = 1/2, 30 mL min^{-1}, and 320 °C. (b) Formation rate resulted from Micro GC over different catalytic systems.

assigned to the C−H bond in adsorbed acetaldehyde species (CH_3CHO^*).[72] After 5 min, bands characteristic of $CH_3CH_2O^*$ (2924, 2963 and 1161 cm^{-1})[39,73] emerged and intensified. The formation of CH_3CHO^* occurs earlier compared to the hydrogenated $CH_3CH_2O^*$ species, consistent with the role of Li in suppressing intermediate hydrogenation. The CH_3CHO^* species can subsequently undergo further hydrogenation to form an ethoxy species ($CH_3CH_2O^*$), and subsequently ethanol.[39,73] Furthermore, bands corresponding to CH_3COO^* (1515 and 1541 cm^{-1}) existed throughout the reaction, commonly observed on the surfaces of Rh-based catalysts with superior ethanol selectivity.[74] Additional bands at 2770, 2723, 1606, and 1342 cm^{-1} corresponded to $HCOO^*$.[75] DRIFT spectra also revealed a minor peak at 2798 cm^{-1} assigned to CH_3O^*,[76] along with a reduction in the intensity of the peak at 2723 cm^{-1} attributable to formate,[77] which are important intermediates of methanol production. Online gas chromatography was used to track and quantify the formation of EtOH and MeOH in the gas phase (Figure 6b). After 10 min, the EtOH formation rate increased compared to that of MeOH, indicating facile CO hydrogenation to CH_3CH_2OH under the specified conditions.

As depicted in Figure 6c, the DRIFTS analysis of the RhO_x/MgO catalysts shows a notable increase in the relative band intensity of unsaturated CH_x^* at 2850 cm^{-1}, in comparison to $RhO_x/Li_2O/MgO$. The observed peaks at 2723 and 1384 cm^{-1} correspond to the characteristic features of adsorbed formate ($HCOO^*$),[39,73] whereas the band centered at 1600 cm^{-1} is associated with the O−C−O vibration (referred to as)[75] of formate species. Furthermore, intense IR bands, at 2798 and 1102 cm^{-1}, representing methoxy groups (CH_3O^*),[75] were detected. The results also revealed that the relative band intensity of CH_3O^* to $HCOO^*$ increased in the unpromoted RhO_x/MgO catalyst, indicating that these intermediates were directly hydrogenated to CH_3OH rather than forming C_{2+} oxygenate intermediates. The results showed a higher absolute amount of adsorbed species on the RhO_x/MgO catalyst. However, these species did not effectively contribute to the formation of the C_{2+} oxygenates. We speculate that the presence of the Li promoter effectively mitigated the formation of methoxy intermediates. A comparison of the data in Figure 6b,d reveals a higher formation rate of ethanol over Rh/Li/MgO than over the Rh/MgO catalysts. The latter showed a significant increase in MeOH production after 15 min compared to EtOH. The enhanced coverage of C_{2+} oxygenate intermediates and reduced concentration of CH_3O^* over the $RhO_x/Li_2O/MgO$ catalyst contributed to the improved EtOH selectivity.

The investigation delved into the impact of varying the support material for RhO_x/Li_2O catalysts, transitioning from MgO to TiO_2, SiO_2, and Al_2O_3, all within identical reaction conditions set at 320 °C and 0.5 MPa. The spectral data, depicted in Figures S10 and 7a, were acquired after the syngas conversion process was conducted on the diverse support matrices. This study aimed to discern the alterations in the catalytic performance and reaction pathways induced by different support materials employed in conjunction with RhO_x/Li_2O catalyst systems. In the depicted Figure 7a, it is evident that the relative band intensity ratio of CH_4 at 3016 cm^{-1} to the unsaturated CH_x^* species at 2924 cm^{-1},[36] exhibits a notable augmentation in the $RhO_x/Li_2O/TiO_2$ catalyst compared to other support materials. This observation underscores the efficacy of TiO_2 as a support in markedly improving the hydrogenation of CH_x^* to CH_4, thereby reducing the coverage of CH_x^* species. Conversely, the relative band intensities corresponding to $HCOO^*$ (2723, 1650, 1606, and 1342 cm^{-1}),[75] along with the CH_3O^* group (2894, 2830, and 1059 cm^{-1}),[76] exhibit a pronounced elevation in the $RhO_x/Li_2O/Al_2O_3$ catalysts, indicative of significant intermediates crucial for methanol production. Furthermore, analysis reveals that the $RhO_x/Li_2O/MgO$ catalyst displayed the highest intensity of $CH_3CH_2O^*$ after 60 min of the reaction, accompanied by the detection of CH_3CHO species, signifying the importance of intermediates for ethanol formation. Among the evaluated catalyst systems, the formation rate (EtOH STY) identified $RhO_x/Li_2O/MgO$ as the catalyst with the highest efficacy for facilitating ethanol synthesis (Figure 7b).

In situ XAS experiments were performed to investigate the structural and chemical characteristics of the $RhO_x/Li_2O/MgO$ catalyst under the reaction conditions at the Rh K-edges, given its significantly enhanced activity and selectivity of ethanol compared to unpromoted RhO_x/MgO (Figure S11a). The structural evolution of the catalyst after H_2 reduction

https://doi.org/10.1021/acscatal.4c05085
ACS Catal. 2025, 15, 2033−2044

under the reaction conditions was probed via EXAFS analysis, whereas alterations in the chemical state were investigated by analyzing the XANES region. The in situ XANES and FT-EXAFS spectra under He flow immediately after the H_2 reduction at 360 °C are shown in Figure S11b and Table S5. No significant changes were observed upon exposure to CO and CO + H_2 gases at ambient pressure, indicating that the chemical state of the Rh species was similar to that of the reduced catalyst.

To further elucidate the role of Li, FTIR spectra were obtained in transmission mode for CO adsorption on the two MgO-based catalysts at low temperature (Figure 8). When CO

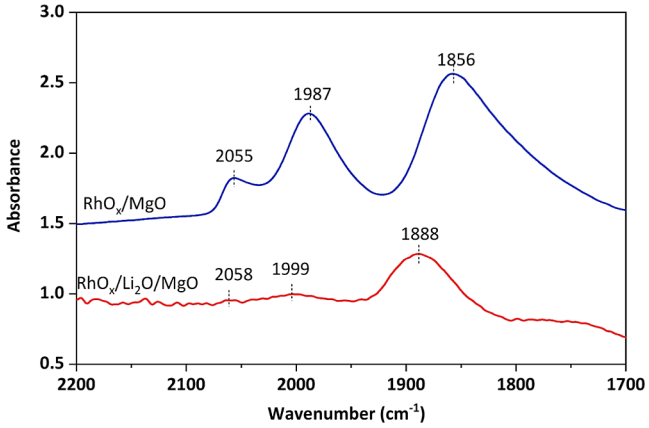

Figure 8. FTIR spectra of CO adsorption for the $RhO_x/Li_2O/MgO$, RhO_x/MgO. Prior to CO adsorption, the catalyst was treated with H_2, and CO was introduced at −20 °C.

was introduced into RhO_x/MgO, three strong adsorption peaks were observed in the region of 1800−2100 cm^{-1} region. The peaks centered in 1856, 1987, and 2055 cm^{-1} can be assigned to CO adsorbed on the hollow site (CO bound to three Rh atoms),[37] bridge site (CO bound to two Rh atoms),[22,45] and on-top site (CO bound to one Rh atom),[22,37] respectively. The addition of Li species to RhO_x/MgO ($RhO_x/Li_2O/MgO$) reduced the absorption capacity for all CO species, indicating a weakening of CO adsorption. Additionally, all peaks shifted toward higher wavenumbers, suggesting changes in the electronic environment of the Rh sites, likely due to electronic effects induced by Li that weaken the metal−CO interaction. It is well-known that back-donation from the metal surface to the adsorbed CO significantly influences to the adsorption strength and the vibrations of the C−O bond.[78,79] The π back-donation contribution is weakened when Rh is positively charged, resulting in weaker adsorption of CO and a shift in the C−O bond vibrational frequency for $RhO_x/Li_2O/MgO$. The adsorption energy of CO was also examined using DFT calculations (Figure S12). E_{ads} of a CO molecule on the $Rh_{13}/MgO(100)$ and $Rh_{13}/Li_2O(111)/MgO(100)$ surfaces were calculated to be −2.34 and −2.02 eV, respectively. It should also be noted that only the on-top sites were considered as adsorption sites in this investigation, and the most stable structures for each model were utilized. This result also suggests that the Li species addition leads to weaker adsorption of CO. When the supported metal nanoparticles become electron-rich, the formation of CH_4 is favored.[80] In the present study, because CH_4 is an undesired byproduct, it is thought that suppressing CH_4 production by making the supported Rh nanoparticles electron-deficient through Li addition would be advantageous for ethanol synthesis. Thus, over $RhO_x/Li_2O/MgO$ catalysts, hydrogenation to CH_4 may be suppressed, and CO species can be more readily inserted into the CH_x−Rh bond, producing C_2 oxygenates more efficiently than on RhO_x/MgO catalysts.

4. CONCLUSION

In this study, we achieved high ethanol production by utilizing MgO as an effective support for Rh catalysts in a syngas-to-ethanol conversion reaction. Among the alkali metals tested, Li was the most favorable promoter for ethanol formation. Through optimization of the reaction conditions, we attained the highest ethanol space-time yield (EtOH STY) of 12.2 mmol g_{cat}^{-1} h^{-1} with a selectivity of 20%. The Li addition as an effective promoter, which likely interacts closely with Rh to form new active sites, enhanced ethanol yield and selectivity. The introduction of Li promoted Rh electron deficiency, suppressed the undesired CH_4 formation and promoted the ethanol formation. In addition, we examined the roles of various catalyst supports (SiO_2, Al_2O_3, and TiO_2) in ethanol synthesis to elucidate their effects. Our findings highlight the significance and implications of MgO as a support for Rh catalysts, offering insights into the design of next-generation catalysts that can upgrade small molecules to chemicals and synthetic fuels.

■ ASSOCIATED CONTENT

Supporting Information

The Supporting Information is available free of charge at https://pubs.acs.org/doi/10.1021/acscatal.4c05085.

Detailed information on the catalytic performance of syngas conversion over various Rh catalysts, XRD patterns and STEM images of $RhO_x/Li_2O/Al_2O_3$, $RhO_x/Li_2O/TiO_2$ and $RhO_x/Li_2O/SiO_2$ catalysts, ex situ Rh K-edge FT-EXAFS spectra of the studied samples, CO_2-TPD curves of MgO and Li_2O/MgO, in situ Rh K-edge XANES and FT-EXAFS spectra of $RhO_x/Li_2O/MgO$, in situ DRIFTS spectra of $RhO_x/Li_2O/Al_2O_3$, $RhO_x/Li_2O/TiO_2$ and $RhO_x/Li_2O/SiO_2$ catalysts, and DFT calculation (Figures S1−S12) (Tables S1−S5) (PDF)

■ AUTHOR INFORMATION

Corresponding Authors

Ken-ichi Shimizu − *Institute for Catalysis, Hokkaido University, Sapporo 001-0021, Japan;* orcid.org/0000-0003-0501-0294; Email: kshimizu@cat.hokudai.ac.jp

Takashi Toyao − *Institute for Catalysis, Hokkaido University, Sapporo 001-0021, Japan;* orcid.org/0000-0002-6062-5622; Email: toyao@cat.hokudai.ac.jp

Authors

Abdellah Ait El Fakir − *Institute for Catalysis, Hokkaido University, Sapporo 001-0021, Japan;* orcid.org/0000-0003-0549-7397

Pengfei Du − *Institute for Catalysis, Hokkaido University, Sapporo 001-0021, Japan*

Li Wan − *Institute for Catalysis, Hokkaido University, Sapporo 001-0021, Japan*

HongLi Pan − *Institute for Catalysis, Hokkaido University, Sapporo 001-0021, Japan*

https://doi.org/10.1021/acscatal.4c05085
ACS Catal. 2025, 15, 2033−2044

Shirun Zhao − *Institute for Catalysis, Hokkaido University, Sapporo 001-0021, Japan*
Nazmul Hasan M.D. Dostagir − *Institute for Catalysis, Hokkaido University, Sapporo 001-0021, Japan;* orcid.org/0000-0002-6656-6539
Akihiko Anzai − *Institute for Catalysis, Hokkaido University, Sapporo 001-0021, Japan*
Shinya Mine − *Research Institute for Chemical Process Technology, National Institute of Advanced Industrial Science and Technology (AIST), Sendai 983-8551, Japan;* orcid.org/0000-0002-8339-0301
Evgeny A. Pidko − *Inorganic Systems Engineering Group, Department of Chemical Engineering, Faculty of Applied Sciences, Delft University of Technology, Delft 2629 HZ, The Netherlands;* orcid.org/0000-0001-9242-9901

Complete contact information is available at: https://pubs.acs.org/10.1021/acscatal.4c05085

Author Contributions

‖A.A.E.F. and P.D. authors contributed equally to this work. This manuscript was collaboratively written by all authors, who have all approved the final version.

Notes

The authors declare no competing financial interest.

■ ACKNOWLEDGMENTS

This study was supported by KAKENHI (23KF0129, 23H01997, 23K20034, and 21H04626) from the Japan Society for the Promotion of Science (JSPS), the JST-FOREST Program (JPMJFR211U), JST-SPRING (JPMJSP2119), and the Joint Usage/Research Center for Catalysis. A.F. gratefully acknowledges support through a JSPS Postdoctoral Fellowship (P23351). XAS measurements were performed at the BL01B1 beamline of SPring-8 at JASRI (2023B2096 and 2023A1931).

■ REFERENCES

(1) Jiao, F.; Bai, B.; Li, G.; Pan, X.; Ye, Y.; Qu, S.; Xu, C.; Xiao, J.; Jia, Z.; Liu, W.; Peng, T.; Ding, Y.; Liu, C.; Li, J.; Bao, X. Disentangling the Activity-Selectivity Trade-off in Catalytic Conversion of Syngas to Light Olefins. *Science* **2023**, *380* (6646), 727−730.
(2) Jiao, F.; Li, J.; Pan, X.; Xiao, J.; Li, H.; Ma, H.; Wei, M.; Pan, Y.; Zhou, Z.; Li, M.; Miao, S.; Li, J.; Zhu, Y.; Xiao, D.; He, T.; Yang, J.; Qi, F.; Fu, Q.; Bao, X. Selective Conversion of Syngas to Light Olefins. *Science* **2016**, *351* (6277), 1065−1068.
(3) Zhong, L.; Yu, F.; An, Y.; Zhao, Y.; Sun, Y.; Li, Z.; Lin, T.; Lin, Y.; Qi, X.; Dai, Y.; Gu, L.; Hu, J.; Jin, S.; Shen, Q.; Wang, H. Cobalt Carbide Nanoprisms for Direct Production of Lower Olefins from Syngas. *Nature* **2016**, *538* (7623), 84−87.
(4) Xu, Y.; Li, X.; Gao, J.; Wang, J.; Ma, G.; Wen, X.; Yang, Y.; Li, Y.; Ding, M. A Hydrophobic FeMn@Si Catalyst Increases Olefins from Syngas by Suppressing C1 By-Products. *Science* **2021**, *371* (6529), 610−613.
(5) van Deelen, T. W.; Hernández Mejía, C.; de Jong, K. P. Control of Metal-Support Interactions in Heterogeneous Catalysts to Enhance Activity and Selectivity. *Nat. Catal.* **2019**, *2* (11), 955−970.
(6) Ma, S.; Huang, S.-D.; Liu, Z.-P. Dynamic Coordination of Cations and Catalytic Selectivity on Zinc−Chromium Oxide Alloys during Syngas Conversion. *Nat. Catal.* **2019**, *2* (8), 671−677.
(7) Ji, Y.; Gao, P.; Zhao, Z.; Xiao, D.; Han, Q.; Chen, H.; Gong, K.; Chen, K.; Han, X.; Bao, X.; Hou, G. Oxygenate-Based Routes Regulate Syngas Conversion over Oxide−Zeolite Bifunctional Catalysts. *Nat. Catal.* **2022**, *5* (7), 594−604.
(8) Chen, Z.; Wang, H.; Liu, Z.; Xu, X. Dynamic and Intermediate-Specific Local Coverage Controls the Syngas Conversion on Rh(111) Surfaces: An *Operando* Theoretical Analysis. *ACS Catal.* **2021**, *11* (7), 3830−3841.
(9) Wang, J.; Liu, Z.; Zhang, R.; Wang, B. Ethanol Synthesis from Syngas on the Stepped Rh(211) Surface: Effect of Surface Structure and Composition. *J. Phys. Chem. C* **2014**, *118* (39), 22691−22701.
(10) Arakawa, H.; Fukushima, T.; Ichikawa, M.; Natsushita, S.; Takeuchi, K.; Matsuzaki, T.; Sugi, Y. SELECTIVE SYNTHESIS OF ETHANOL OVER Rh−Ti−Fe−Ir/SiO_2CATALYST AT HIGH PRESSURE SYNGAS CONVERSION. *Chem. Lett.* **1985**, *14* (7), 881−884.
(11) Ichikawa, M.; Fukushima, T. Mechanism of Syngas Conversion into C_2-Oxygenates Such as Ethanol Catalysed on a SiO_2 -Supported Rh−Ti Catalyst. *J. Chem. Soc., Chem. Commun.* **1985**, No. 6, 321−323.
(12) Sachtler, W. M. H.; Ichikawa, M. Catalytic Site Requirements for Elementary Steps in Syngas Conversion to Oxygenates over Promoted Rhodium. *J. Phys. Chem.* **1986**, *90* (20), 4752−4758.
(13) Subramani, V.; Gangwal, S. K. A Review of Recent Literature to Search for an Efficient Catalytic Process for the Conversion of Syngas to Ethanol. *Energy Fuels* **2008**, *22* (2), 814−839.
(14) Kang, J.; He, S.; Zhou, W.; Shen, Z.; Li, Y.; Chen, M.; Zhang, Q.; Wang, Y. Single-Pass Transformation of Syngas into Ethanol with High Selectivity by Triple Tandem Catalysis. *Nat. Commun.* **2020**, *11* (1), 827.
(15) Spivey, J. J.; Egbebi, A. Heterogeneous Catalytic Synthesis of Ethanol from Biomass-Derived Syngas. *Chem. Soc. Rev.* **2007**, *36* (9), 1514.
(16) Gupta, M.; Smith, M. L.; Spivey, J. J. Heterogeneous Catalytic Conversion of Dry Syngas to Ethanol and Higher Alcohols on Cu-Based Catalysts. *ACS Catal.* **2011**, *1* (6), 641−656.
(17) Ao, M.; Pham, G. H.; Sunarso, J.; Tade, M. O.; Liu, S. Active Centers of Catalysts for Higher Alcohol Synthesis from Syngas: A Review. *ACS Catal.* **2018**, *8* (8), 7025−7050.
(18) Mäki-Arvela, P.; Aho, A.; Simakova, I.; Yu Murzin, D. Sustainable Aviation Fuel from Syngas through Higher Alcohols. *ChemCatChem* **2022**, *14* (23), No. e202201005.
(19) Xiang, Y.; Barbosa, R.; Kruse, N. Higher Alcohols through CO Hydrogenation over CoCu Catalysts: Influence of Precursor Activation. *ACS Catal.* **2014**, *4* (8), 2792−2800.
(20) Li, X.; San, X.; Zhang, Y.; Ichii, T.; Meng, M.; Tan, Y.; Tsubaki, N. Direct Synthesis of Ethanol from Dimethyl Ether and Syngas over Combined H-Mordenite and Cu/ZnO Catalysts. *ChemSusChem* **2010**, *3* (10), 1192−1199.
(21) Cao, A.; Liu, G.; Wang, L.; Liu, J.; Yue, Y.; Zhang, L.; Liu, Y. Growing Layered Double Hydroxides on CNTs and Their Catalytic Performance for Higher Alcohol Synthesis from Syngas. *J. Mater. Sci.* **2016**, *51* (11), 5216−5231.
(22) Feng, Y.; Zhang, Y.; Wang, J.; Ling, L.; Zhang, R.; Fan, M.; Hou, B.; Li, D.; Wang, B. Promotion of Anatase/Rutile Junction to Direct Conversion of Syngas to Ethanol on the Rh/TiO_2 Catalysts. *ACS Catal.* **2024**, *14* (3), 1874−1881.
(23) Bordoloi, A.; Anton, J.; Ruland, H.; Muhler, M.; Kaluza, S. Metal−Support Interactions in Surface-Modified Cu−Co Catalysts Applied in Higher Alcohol Synthesis. *Catal. Sci. Technol.* **2015**, *5* (7), 3603−3612.
(24) Sun, J.; Cai, Q.; Wan, Y.; Wan, S.; Wang, L.; Lin, J.; Mei, D.; Wang, Y. Promotional Effects of Cesium Promoter on Higher Alcohol Synthesis from Syngas over Cesium-Promoted Cu/ZnO/Al_2O_3 Catalysts. *ACS Catal.* **2016**, *6* (9), 5771−5785.
(25) Asundi, A. S.; Hoffman, A. S.; Bothra, P.; Boubnov, A.; Vila, F. D.; Yang, N.; Singh, J. A.; Zeng, L.; Raiford, J. A.; Abild-Pedersen, F.; Bare, S. R.; Bent, S. F. Understanding Structure−Property Relationships of MoO_3 -Promoted Rh Catalysts for Syngas Conversion to Alcohols. *J. Am. Chem. Soc.* **2019**, *141* (50), 19655−19668.
(26) Yang, N.; Yoo, J. S.; Schumann, J.; Bothra, P.; Singh, J. A.; Valle, E.; Abild-Pedersen, F.; Nørskov, J. K.; Bent, S. F. Rh-MnO Interface Sites Formed by Atomic Layer Deposition Promote Syngas Conversion to Higher Oxygenates. *ACS Catal.* **2017**, *7* (9), 5746−5757.

(27) Huang, X.; Teschner, D.; Dimitrakopoulou, M.; Fedorov, A.; Frank, B.; Kraehnert, R.; Rosowski, F.; Kaiser, H.; Schunk, S.; Kuretschka, C.; Schlögl, R.; Willinger, M.; Trunschke, A. Atomic-Scale Observation of the Metal−Promoter Interaction in Rh-Based Syngas-Upgrading Catalysts. *Angew. Chem., Int. Ed.* **2019**, *58* (26), 8709−8713.
(28) Yang, N.; Medford, A. J.; Liu, X.; Studt, F.; Bligaard, T.; Bent, S. F.; Nørskov, J. K. Intrinsic Selectivity and Structure Sensitivity of Rhodium Catalysts for C_{2+} Oxygenate Production. *J. Am. Chem. Soc.* **2016**, *138* (11), 3705−3714.
(29) Granlund, M. Z.; Jansson, K.; Nilsson, M.; Dawody, J.; Pettersson, L. J. Evaluation of Co, La, and Mn Promoted Rh Catalysts for Autothermal Reforming of Commercial Diesel: Aging and Characterization. *Appl. Catal., B* **2015**, *172*−*173*, 145−153.
(30) Nathan, S. S.; Asundi, A. S.; Hoffman, A. S.; Hong, J.; Zhou, C.; Vila, F. D.; Cargnello, M.; Bare, S. R.; Bent, S. F. Surface Fe Clusters Promote Syngas Reaction to Oxygenates on Rh Catalysts Modified by Atomic Layer Deposition. *J. Catal.* **2022**, *414*, 125−136.
(31) Liu, Y.; Göeltl, F.; Ro, I.; Ball, M. R.; Sener, C.; Aragão, I. B.; Zanchet, D.; Huber, G. W.; Mavrikakis, M.; Dumesic, J. A. Synthesis Gas Conversion over Rh-Based Catalysts Promoted by Fe and Mn. *ACS Catal.* **2017**, *7* (7), 4550−4563.
(32) Zhong, H.; Wang, J.; Guo, S.; Fang, K.; Liu, Y. Mutual Tailored Bimetallic Rh−Co Supported on La Modified SiO_2 for Direct Ethanol Synthesis from Syngas. *Ind. Eng. Chem. Res.* **2019**, *58* (8), 2631−2643.
(33) Mu, Y.; Zheng, J.; Yang, Q.; Liu, G.; Liu, X.; Wang, X.; Wang, G.; Liang, X.; Yuan, Y. Active Site Synergy of Rh and Co Derived from ZrO_2 -Supported $LaRh_xCo_{1-x}O_3$ Perovskite Nanostructures for the Direct Synthesis of Ethanol from Syngas. *ACS Appl. Nano Mater.* **2023**, *6* (7), 5692−5702.
(34) Zhao, W.; Guan, Z.; Li, D.; Wang, B.; Fan, M.; Zhang, R. Syngas Conversion to C_2 Species over WC and M/WC (M = Cu or Rh) Catalysts: Identifying the Function of Surface Termination and Supported Metal Type. *ACS Appl. Mater. Interfaces* **2022**, *14* (17), 19491−19504.
(35) Subramanian, N. D.; Gao, J.; Mo, X.; Goodwin, Jr. J. G.; Torres, W.; Spivey, J. J. La and/or V Oxide Promoted Rh/SiO_2 Catalysts: Effect of Temperature, H_2/CO Ratio, Space Velocity, and Pressure on Ethanol Selectivity from Syngas. *J. Catal.* **2010**, *272* (2), 204−209.
(36) Egbebi, A.; Schwartz, V.; Overbury, S. H.; Spivey, J. J. Effect of Li Promoter on Titania-Supported Rh Catalyst for Ethanol Formation from CO Hydrogenation. *Catal. Today* **2010**, *149* (1−2), 91−97.
(37) Schwartz, V.; Campos, A.; Egbebi, A.; Spivey, J. J.; Overbury, S. H. EXAFS and FT-IR Characterization of Mn and Li Promoted Titania-Supported Rh Catalysts for CO Hydrogenation. *ACS Catal.* **2011**, *1* (10), 1298−1306.
(38) Xu, D.; Ding, M.; Hong, X.; Liu, G. Mechanistic Aspects of the Role of K Promotion on Cu−Fe-Based Catalysts for Higher Alcohol Synthesis from CO_2 Hydrogenation. *ACS Catal.* **2020**, *10* (24), 14516−14526.
(39) Zeng, Z.; Li, Z.; Guan, T.; Guo, S.; Hu, Z.; Wang, J.; Rykov, A.; Lv, J.; Huang, S.; Wang, Y.; Ma, X. CoFe Alloy Carbide Catalysts for Higher Alcohols Synthesis from Syngas: Evolution of Active Sites and Na Promoting Effect. *J. Catal.* **2022**, *405*, 430−444.
(40) Katzer, J. R.; Sleight, A. W.; Gajardo, P.; Michel, J. B.; Gleason, E. F.; McMillan, S. The Role of the Support in CO Hydrogenation Selectivity of Supported Rhodium. *Faraday Discuss. Chem. Soc.* **1981**, *72*, 121.
(41) Solymosi, F. Hydrogenation of CO on Supported Rh Catalysts. *J. Catal.* **1982**, *75* (1), 78−93.
(42) Yu, J.; Mao, D.; Han, L.; Guo, Q.; Lu, G. Catalytic Conversion of Syngas into C_{2+} Oxygenates over Rh/SiO_2-Based Catalysts: The Remarkable Effect of Hydroxyls on the SiO_2. *J. Mol. Catal. A:Chem.* **2013**, *367*, 38−45.
(43) Camposeco, R.; Castillo, S.; Hinojosa-Reyes, M.; Zanella, R.; López-Curiel, J. C.; Fuentes, G. A.; Mejía-Centeno, I. Active TiO_2-Nanostructured Surfaces for CO Oxidation on Rh Model Catalysts at Low-Temperature. *Catal. Lett.* **2019**, *149* (6), 1565−1578.
(44) Yu, J.; Yu, J.; Shi, Z.; Guo, Q.; Xiao, X.; Mao, H.; Mao, D. The Effects of the Nature of TiO_2 Supports on the Catalytic Performance of Rh−Mn/TiO_2 Catalysts in the Synthesis of C_2 Oxygenates from Syngas. *Catal. Sci. Technol.* **2019**, *9* (14), 3675−3685.
(45) Kusama, H.; Okabe, K.; Sayama, K.; Arakawa, H. CO_2 Hydrogenation to Ethanol over Promoted Rh/SiO2 Catalysts. *Catal. Today* **1996**, *28* (3), 261−266.
(46) Jing, Y.; He, C.; Zhang, N.; Murano, Y.; Toyoshima, R.; Kondoh, H.; Kageyama, Y.; Inomata, H.; Toyao, T.; Shimizu, K. Promotional Effect of Ag on the Catalytic Decomposition of N_2O in the Presence of O_2 over the Al_2O_3 -Supported Rh Catalyst. *ACS Catal.* **2023**, *13* (19), 12983−12993.
(47) Jing, Y.; Taketoshi, K.; Zhang, N.; He, C.; Toyao, T.; Maeno, Z.; Ohori, T.; Ishikawa, N.; Shimizu, K. Catalytic Decomposition of N_2O in the Presence of O_2 through Redox of Rh Oxide in a RhO_x/ZrO_2 Catalyst. *ACS Catal.* **2022**, *12* (11), 6325−6333.
(48) Zhang, N.; He, C.; Jing, Y.; Qian, Y.; Toyao, T.; Shimizu, K. Enhanced N_2O Decomposition on Rh/ZrO_2 Catalysts through the Promotional Effect of Palladium. *Surf. Interfaces* **2024**, *46*, 104120.
(49) Wu, D.; Liu, S.; Zhong, M.; Zhao, J.; Du, C.; Yang, Y.; Sun, Y.; Lin, J.; Wan, S.; Wang, S.; Huang, J.; Yao, Y.; Li, Z.; Xiong, H. Nature and Dynamic Evolution of Rh Single Atoms Trapped by CeO_2 in CO Hydrogenation. *ACS Catal.* **2022**, *12* (19), 12253−12267.
(50) Ravel, B.; Newville, M. ATHENA, ARTEMIS, HEPHAESTUS: Data Analysis for X-Ray Absorption Spectroscopy Using IFEFFIT. *J. Synchrotron Radiat.* **2005**, *12* (4), 537−541.
(51) Kresse, G.; Furthmüller, J. Efficient Iterative Schemes for *Ab Initio* Total-Energy Calculations Using a Plane-Wave Basis Set. *Phys. Rev. B* **1996**, *54* (16), 11169−11186.
(52) Kresse, G.; Furthmüller, J. Efficiency of Ab-Initio Total Energy Calculations for Metals and Semiconductors Using a Plane-Wave Basis Set. *Comput. Mater. Sci.* **1996**, *6* (1), 15−50.
(53) Perdew, J. P.; Ruzsinszky, A.; Csonka, G. I.; Vydrov, O. A.; Scuseria, G. E.; Constantin, L. A.; Zhou, X.; Burke, K. Restoring the Density-Gradient Expansion for Exchange in Solids and Surfaces. *Phys. Rev. Lett.* **2008**, *100* (13), 136406.
(54) Blöchl, P. E. Projector Augmented-Wave Method. *Phys. Rev. B* **1994**, *50* (24), 17953−17979.
(55) Grimme, S.; Ehrlich, S.; Goerigk, L. Effect of the Damping Function in Dispersion Corrected Density Functional Theory. *J. Comput. Chem.* **2011**, *32* (7), 1456−1465.
(56) Hinuma, Y.; Toyao, T.; Kamachi, T.; Maeno, Z.; Takakusagi, S.; Furukawa, S.; Takigawa, I.; Shimizu, K. Density Functional Theory Calculations of Oxygen Vacancy Formation and Subsequent Molecular Adsorption on Oxide Surfaces. *J. Phys. Chem. C* **2018**, *122* (51), 29435−29444.
(57) Chuang, S. The Effect of Alkali Promotion on CO Hydrogenation over Rh/TiO_2. *J. Catal.* **1985**, *95* (2), 435−446.
(58) Liu, G.; Yang, G.; Peng, X.; Wu, J.; Tsubaki, N. Recent Advances in the Routes and Catalysts for Ethanol Synthesis from Syngas. *Chem. Soc. Rev.* **2022**, *51* (13), 5606−5659.
(59) Luk, H. T.; Mondelli, C.; Ferré, D. C.; Stewart, J. A.; Pérez-Ramírez, J. Status and Prospects in Higher Alcohols Synthesis from Syngas. *Chem. Soc. Rev.* **2017**, *46* (5), 1358−1426.
(60) Behrendt, G.; Mockenhaupt, B.; Prinz, N.; Zobel, M.; Ras, E.; Behrens, M. CO Hydrogenation to Methanol over Cu/MgO Catalysts and Their Synthesis from Amorphous Magnesian Georgeite Precursors. *ChemCatChem* **2022**, *14* (17), No. e202200299.
(61) Cao, A.; Wang, Z.; Li, H.; Elnabawy, A. O.; Nørskov, J. K. New Insights on CO and CO_2 Hydrogenation for Methanol Synthesis: The Key Role of Adsorbate-Adsorbate Interactions on Cu and the Highly Active MgO-Cu Interface. *J. Catal.* **2021**, *400*, 325−331.
(62) He, C.; Ruan, T.; Ouyang, X.; Ma, Y.; Qian, Y.; Qiu, X. Selective Hydrodeoxygenation of Monophenolics from Lignin Bio-Oil for Preparing Cyclohexanol and Its Derivatives over Ni-Co/Al_2O_3-MgO Catalyst. *Ind. Crops Prod.* **2023**, *202*, 117045.
(63) Ahmed, S.; Irshad, M.; Yoon, W.; Karanwal, N.; Sugiarto, J. R.; Khan, M. K.; Kim, S. K.; Kim, J. Evaluation of MgO as a Promoter for

https://doi.org/10.1021/acscatal.4c05085
ACS Catal. 2025, 15, 2033−2044

the Hydrogenation of CO_2 to Long-Chain Hydrocarbons over Fe-Based Catalysts. *Appl. Catal., B* **2023**, *338*, 123052.
(64) Fang, H.; Wu, S.; Ayvali, T.; Zheng, J.; Fellowes, J.; Ho, P.-L.; Leung, K. C.; Large, A.; Held, G.; Kato, R.; Suenaga, K.; Reyes, Y. I. A.; Thang, H. V.; Chen, H.-Y. T.; Tsang, S. C. E. Dispersed Surface Ru Ensembles on MgO(111) for Catalytic Ammonia Decomposition. *Nat. Commun.* **2023**, *14* (1), 647.
(65) Wang, H. Y.; Ruckenstein, E. Carbon Dioxide Reforming of Methane to Synthesis Gas over Supported Rhodium Catalysts: The Effect of Support. *Appl. Catal., A* **2000**, *204* (1), 143−152.
(66) Yoshida, H.; Yazawa, Y.; Hattori, T. Effects of Support and Additive on Oxidation State and Activity of Pt Catalyst in Propane Combustion. *Catal. Today* **2003**, *87* (1−4), 19−28.
(67) Yoshida, H.; Nonoyama, S.; Yazawa, Y.; Hattori, T. Stabilization of High Oxidation State of Platinum over Basic Support Oxide Examined by in Situ Laboratory XANES and Temperature Programmed Desorption of Oxygen. *Catal. Today* **2010**, *153* (3−4), 156−161.
(68) Beyer, H.; Emmerich, J.; Chatziapostolou, K.; Köhler, K. Decomposition of Nitrous Oxide by Rhodium Catalysts: Effect of Rhodium Particle Size and Metal Oxide Support. *Appl. Catal., A* **2011**, *391* (1−2), 411−416.
(69) Beale, A. M.; Weckhuysen, B. M. EXAFS as a Tool to Interrogate the Size and Shape of Mono and Bimetallic Catalyst Nanoparticles. *Phys. Chem. Chem. Phys.* **2010**, *12* (21), 5562.
(70) Marinkovic, N.; Sasaki, K.; Adzic, R. Nanoparticle Size Evaluation of Catalysts by EXAFS: Advantages and Limitations. *Zast. Mater.* **2016**, *57* (1), 101−109.
(71) Li, Z.; Hu, Z.; Zeng, Z.; Guo, S.; Lv, J.; Huang, S.; Wang, Y.; Ma, X. Lamellar-Structured Silicate Derived Highly Dispersed CoCu Catalyst for Higher Alcohol Synthesis from Syngas. *Ind. Eng. Chem. Res.* **2022**, *61* (20), 6859−6871.
(72) Prieto, G.; Concepción, P.; Martínez, A.; Mendoza, E. New Insights into the Role of the Electronic Properties of Oxide Promoters in Rh-Catalyzed Selective Synthesis of Oxygenates from Synthesis Gas. *J. Catal.* **2011**, *280* (2), 274−288.
(73) Zeng, Z.; Li, Z.; Guo, S.; Lv, J.; Huang, S.; Wang, Y.; Ma, X. Janus Au−$Fe_{2.2}C$ Catalyst for Direct Conversion of Syngas to Higher Alcohols. *ACS Sustain. Chem. Eng.* **2021**, *9* (33), 11258−11268.
(74) Bwoker, M. On the Mechanism of Ethanol Synthesis on Rhodium. *Catal. Today* **1992**, *15* (1), 77−100.
(75) Zeng, Z.; Li, Z.; Kang, L.; Han, X.; Qi, Z.; Guo, S.; Wang, J.; Rykov, A.; Lv, J.; Wang, Y.; Ma, X. A Monodisperse ε'-$(Co_x Fe_{1-x})_{2.2}$C Bimetallic Carbide Catalyst for Direct Conversion of Syngas to Higher Alcohols. *ACS Catal.* **2022**, *12* (10), 6016−6028.
(76) Wang, Y.; Kattel, S.; Gao, W.; Li, K.; Liu, P.; Chen, J. G.; Wang, H. Exploring the Ternary Interactions in Cu−ZnO−ZrO_2 Catalysts for Efficient CO_2 Hydrogenation to Methanol. *Nat. Commun.* **2019**, *10* (1), 1166.
(77) Wu, C.; Lin, L.; Liu, J.; Zhang, J.; Zhang, F.; Zhou, T.; Rui, N.; Yao, S.; Deng, Y.; Yang, F.; Xu, W.; Luo, J.; Zhao, Y.; Yan, B.; Wen, X.-D.; Rodriguez, J. A.; Ma, D. Inverse ZrO_2/Cu as a Highly Efficient Methanol Synthesis Catalyst from CO_2 Hydrogenation. *Nat. Commun.* **2020**, *11* (1), 5767.
(78) Zeinalipour-Yazdi, C. D.; Cooksy, A. L.; Efstathiou, A. M. CO Adsorption on Transition Metal Clusters: Trends from Density Functional Theory. *Surf. Sci.* **2008**, *602* (10), 1858−1862.
(79) Gajdo, M.; Eichler, A.; Hafner, J. CO Adsorption on Close-Packed Transition and Noble Metal Surfaces: Trends from *Ab Initio* Calculations. *J. Phys.: Condens. Matter* **2004**, *16* (8), 1141−1164.
(80) Tian, X.; Wang, T.; Yang, Y.; Li, Y.-W.; Wang, J.; Jiao, H. About Copper Promotion in CH_4 Formation from CO Hydrogenation on Fe(100): A Density Functional Theory Study. *Appl. Catal., A* **2017**, *530*, 83−92.

https://doi.org/10.1021/acscatal.4c05085
ACS Catal. 2025, 15, 2033−2044